FastLink: An Efficient Initial Access Protocol for Millimeter Wave Systems

Irmak Aykin
University of Arizona
Tucson, AZ
aykin@email.arizona.edu

Marwan Krunz[*]
University of Arizona
Tucson, AZ
krunz@email.arizona.edu

ABSTRACT

To overcome the high propagation loss and satisfy a given link budget, millimeter wave (mmW) communication systems rely on highly directional antennas, both at the base station (BS) and the user equipment (UE). Due to this directionality, initial access (IA) and association can be particularly challenging. Existing approaches for IA in directional networks suffer from long discovery time and/or high misdetection probability of the UE. In this paper, we propose FastLink, an efficient IA protocol for mmW systems with electronically steerable antennas. FastLink always transmits/receives using the narrowest possible beam, allowing high beamforming gains and low misdetection rate. It uses a unique binary-search-based algorithm, called 3DPF, to scan only a small subset of the angular space and find in logarithmic time the best transmit-receive beam pair. We formulate the beam-finding process as a sparse problem, exploiting the poor scattering nature of mmW channels. Compressive sensing is then used to determine the minimum number of measurements needed to reconstruct the sparse channel. 3DPF is incorporated into FastLink to establish the directional link, and the required messaging between the BS and the UE is explained in detail. For performance evaluation purposes, we first conduct simulations based on NYU mmW channel model and then experiment with a custom mmW testbed utilizing uniform planar arrays and operating at 29 GHz frequency. Our extensive simulations and hardware experiments verify the efficiency of FastLink, and show that 3DPF can reduce the search time by $65 - 99\%$ compared to 802.11ad-like beam finding scheme.

KEYWORDS

Millimeter wave, beam finding, initial access, directional communications, compressive sensing, analog beamforming.

[*]Also with Dept. of EDE, University of Technology Sydney, Australia.

1 INTRODUCTION

The abundant mmW spectrum is vital to meeting the high demands of next-generation wireless technologies, including 5G cellular systems [1], WLANs (e.g., WiGig [16]), internet of things (IoT), and connected and autonomous vehicles. However, extending wireless communications to mmW bands faces many challenges, such as high channel losses [6, 18], poor penetration through dry walls and human body, and atmospheric absorption at certain mmW frequencies [19]. These challenges limit signal coverage and hinder communications. On the other hand, due to the much smaller wavelengths at mmW frequencies, many antenna elements can be packed into a single device without increasing its form factor. With proper processing of signals fed into these antennas, transmissions can be beamed along a desired direction. The severe signal attenuation in the mmW bands can then be compensated for by the beamforming gain obtained with the use of antenna arrays [4].

Depending on the beamforming architecture, the beamforming weights that are used to focus the signal in a desired direction could be applied in the digital and/or analog domain. Digital beamforming multiplies a particular coefficient (i.e., beamforming weights) by the modulated baseband signal of a given RF chain. Analog beamforming, on the other hand, applies complex coefficients to alter the RF signals by controlling phase shifters [20]. Finally, in hybrid (analog/digital) beamforming, the signal processing is divided between the analog and digital domains, allowing a comparable performance to digital beamforming but with fewer RF chains [12]. The high cost and power consumption of having multiple RF chains force mmW systems to rely heavily on analog beamforming.

However, the increase in the spatial reuse due to highly directional communications comes at the cost of complicating various control functions, including the initial access (IA) procedure [19]. IA allows a user equipment (UE) to establish a connection with a base station (BS). In current 4G LTE systems, IA is performed in an omnidirectional fashion, which alleviates the burden of beam alignment. Beamforming or other directional transmissions can be performed after initial link establishment. However, in mmW frequencies, the IA procedure must be done directionally to allow the UE to determine suitable initial directions for transmission. This directional search delays the link establishment, lowers throughput and reduces the bandwidth efficiency of mmW bands [13].

In this paper, we propose an efficient IA protocol called FastLink for mmW systems. FastLink allows devices to transmit/receive using the narrowest possible beams, and hence providing the highest possible beamforming gains. At the same time, the beam directions are switched in such a way that BS/UE beam alignment can be achieved in much shorter time compared to other search mechanisms used in the 802.11ad standard and 5G New Radio (NR).

FastLink aims at identifying the best transmit and receive beams in an efficient way, exploiting channel sparsity. We first use compressive sensing (CS) to determine the number of measurements (beam probes) needed to find the "dominant" cluster. Then, using this insight, we design a binary-search-based algorithm, called 3DPF, to find the best transmit-receive beam pair in 3D. 3DPF divides the set of beam directions into equally spaced subsets and then finds the beam that achieves the maximum received power in each subset. The number of subsets is a parameter that we determine using CS.

The contributions of this paper can be summarized as follows:

- Utilizing CS methods, we show how to obtain the optimal beam direction using a small number of measurements that is logarithmic in the total number of possible beams.
- We develop a novel 3D beam scanning algorithm, 3DPF, based on beam subset partitioning and binary search, which allows mmW devices to discover each other directionally while keeping the discovery time and the UE misdetection probability low.
- We integrate the proposed beam-finding algorithm into an IA protocol, called FastLink, and we explain the required control messages that need to be exchanged between the BS and the UE.
- We verify the efficiency of 3DPF by conducting extensive MATLAB simulations as well as hardware experiments on a custom-built testbed. Our simulations implement the NYU channel model [4] with modifications to account for more realistic small scale effects. Our hardware setup is comprised of a mmW signal generator, vector signal analyzer, and 4×4 cross-cross polarized uniform planar arrays. We run the experiments in the 29 GHz band, collecting the received signal strength (RSS) measurements and timing results.

The experiments are conducted in an indoor office environment, testing both line-of-sight (LOS) and non-line-of-sight (NLOS) conditions. Our hardware experiments and simulation results indicate that 3DPF reduces the search time by more than 65% compared to 802.11ad-like beam search, and yet achieves the same misdetection probability.

2 RELATED WORK

For mmW systems that rely on analog beamforming, three main approaches for IA have been discussed in the literature: Exhaustive search [1], two-stage hierarchical search [16], and context-information-based (CI-based) search [3]. Exhaustive search is a brute-force sequential beam searching technique that is proposed for 5G NR [14]. In the 5G IA, the BS sequentially transmits synchronization signals along different directions to allow undiscovered UEs to detect one of the BS's transmit beams [1]. This exhaustive search comes at the cost of significant discovery time, as each transmit/receive pair must be probed sequentially. On the other hand, two-stage scanning used in the 802.11ad standard employs a hierarchical multi-resolution beamforming codebook to expedite IA. In the first phase, the access point (AP) sequentially transmits synchronization signals over wider (quasi-omnidirectional) sectors and tries to determine the best coarse direction. In the second phase (beam refinement), the AP refines its search within the best coarse sector by switching to narrow beams [16]. Although this approach

reduces the IA delay, the search time still scales linearly with the number of narrow beams. Finally, in CI-based search, the UE simply selects the optimal beam direction based on GPS information [13].

Alternative IA approaches to the above have been proposed in the literature. The authors in [2] used a unique approach based on hashing functions to identify the best beam. Although the hash functions reduce the search time, the resulting beamforming gains are lower than that of a single beam, leading to a higher misdetection probability. In [15], the authors proposed a beamforming scheme that exploits the correlation between the sub-6 GHz and the mmW interfaces to provide efficient beam alignment. Although they improve the performance, their scheme requires a dedicated sub-6 GHz channel, which may not be feasible for all mmW systems. Finally, the authors in [22] proposed a model-driven beam-steering scheme called OScan, which reduces the search latency. However, their design is based on mmW channel measurements obtained using horn antennas. In reality, horn antennas have significantly different characteristics than phased-array antennas.

The aforementioned techniques present different tradeoffs between *discovery time* (time to establish directional communication between the BS and the UE) and *misdetection probability*. The misdetection probability is the probability that a UE is not being detected by the BS. In its first phase, the 802.11ad scheme scans the space using wide beams, and thus achieves a low discovery time. However, it also has a high chance of missing users due to low beamforming gains. With the beam refinement phase (phase 2), 802.11ad scheme attains better coverage and can even reach users located at the cell edge, but this comes at the expense of much higher discovery time.

Recently, CS has gained great attention as a means to exploit the sparsity of mmW channels [5, 11]. Essentially, CS is a signal processing technique that can be used to efficiently reconstruct a signal by solving an underdetermined set of linear equations. It is based on the principle that signal sparsity can be exploited to recover the signal using far fewer samples than required by the Shannon-Nyquist sampling theorem [10]. This idea has been applied in [5] for mmW channel estimation, where the authors used it to design analog beamformers. Similarly, the authors in [8] described a CS-based approach to estimate multipath channels (not necessarily mmW) that have a sparse representation, without imposing analog beamforming constraints. In [11], the authors also utilized CS in a multiuser MIMO system to design beamformers in a way that effectively mitigates interference. While these analyses corroborate the significance of CS for channel estimation, they do not specify a practical way for collecting the required measurements and consider the algorithmic aspect of IA.

To obviate the shortcomings mentioned above, here we develop a practical algorithm based on CS, which reduces the beam searching delay while achieving a very low misdetection probability. Our algorithm handles the IA completely in mmW bands. In addition, both the analysis and the experiments utilize phased-array antennas, which is the enabling technology for mmW communications.

3 BEAMFORMING IN ANTENNA ARRAYS

We consider the IA process between a BS and a single UE, with electronically steerable phased-array antennas at both ends. In addition, we assume analog beamforming for both the BS and the UE, as it is

the most energy-efficient beamforming solution currently available. Without loss of generality, we let the BS be the transmitter (Tx) and UE be the receiver (Rx). In this section, we focus on the UE side (Rx). Extension to the BS is straightforward. For simplicity, we do not use subscripts to denote BS and UE.

Before we invoke on the algorithmic details of our IA design, we first explain how phased-array antennas can be steered towards a desired direction. To electronically steer the beam, complex weights should be applied to each antenna element in the array. To determine these weights, we first calculate the array factors (AFs) of the BS and UE antenna arrays. AF is the factor by which the element factor of an individual antenna is multiplied to get the firing pattern of the entire array. We start by analyzing a uniform linear array (ULA) and then extend the analysis to a uniform planar array (UPA).

Let N and F_{ULA} denote the number of antennas and the array factor for a ULA, where the array receives a signal from a plane wave at an incident angle θ (relative to the plane of the array). Because the transmission paths are not equal, the received signal has different phase shifts at different antenna elements. For a ULA, adjacent elements are separated by the same distance d, leading to a linear array of total length $(N-1)d$. Note that the phase of antenna element n leads the phase of element $n-1$ by $\frac{2\pi}{\lambda}d\cos\theta$, where λ is the wavelength of the signal. Thus, we can write the received signal at antenna n, $n \in \{1, \cdots, N\}$, as:

$$s_n = R\, I_n\, e^{jdn\frac{2\pi}{\lambda}\cos\theta} \tag{1}$$

where I_n is the amplitude excitation of the nth element and R is the radiation pattern of each antenna element. As I_n does not affect the analog beamforming weights, for simplicity, we assume $I_n = 1$.

Let the output of the antenna array, s, be a weighted sum of s_n's, with each term s_n multiplied by a complex weight w_n:

$$s = R\sum_{n=1}^{N} w_n e^{jdn\frac{2\pi}{\lambda}\cos\theta} = R\, F_{\mathrm{ULA}}. \tag{2}$$

Assuming the same signal magnitude at each antenna, F_{ULA} can be maximized by selecting w_n in a way to ensure that the received signals are in phase, i.e., by setting $w_n = e^{-jdn\frac{2\pi}{\lambda}\cos\theta}$. To achieve that, the phase of the signal received by the Nth antenna is kept the same, and the phase of the signal received by every other antenna element n, $n = 1, \cdots, N-1$, is shifted by $(N-n)\gamma = (N-n)\frac{2\pi}{\lambda}d\cos\theta$.

Now consider a UPA with a horizontal inter-element distance d_x, vertical inter-element distance d_y, and the AF denoted as F_{UPA}. Suppose that the incident wave of the received signal arrives from polar angle θ and azimuth angle α, and the antennas are placed on an $M \times N$ 2D grid. Following a similar analysis, we can write the received signal at antenna element (m, n), $s_{m,n}$ as:

$$s_{m,n} = R\, e^{j\frac{2\pi}{\lambda}(d_x m\cos\alpha\sin\theta + d_y n\sin\alpha\sin\theta)} \tag{3}$$

where $m \in \{1, \cdots, M\}$ and $n \in \{1, \cdots, N\}$. Similarly, the received signal s after beamforming with complex phase-shift weights $w_{m,n}$ can be written as:

$$s = R\sum_{m=1}^{M}\sum_{n=1}^{N} w_{m,n} e^{j\frac{2\pi}{\lambda}(d_x m\cos\alpha\sin\theta + d_y n\sin\alpha\sin\theta)} = R\, F_{\mathrm{UPA}} \tag{4}$$

Complex beamformer weights can then be calculated as $w_{m,n} = e^{-j\frac{2\pi}{\lambda}(d_x m\cos\alpha\sin\theta + d_y n\sin\alpha\sin\theta)}$.

4 CS-BASED BEAM FINDING

Because of the few reflections in mmW communications, the channel matrix between the BS and the UE is sparse [4, 7]. More specifically, a transmitted signal reaches the Rx along a few AoA clusters, depending on the environment (see for example, the received power profile in Fig. 5 in Section 7.1). CS has been widely used in the literature to capture and represent sparse signals at a rate significantly below the Nyquist rate [5, 10]. Considering the limited scattering nature of the mmW channel, in this section, we formulate the channel estimation problem as a sparse problem. We then show how CS can be used to find the optimal beam direction.

First, we express the channel between a BS and a UE under UPAs. To denote a matrix of x rows and y columns, we use the notation $x \times y$. Let the total number of antennas at the BS and the UE be $A_{\mathrm{BS}} = M_{\mathrm{BS}}N_{\mathrm{BS}}$ and $A_{\mathrm{UE}} = M_{\mathrm{UE}}N_{\mathrm{UE}}$, respectively. Here, M_i and N_i, $i \in \{\mathrm{BS}, \mathrm{UE}\}$, refer to the number of rows and columns in the UPA. Let $\mathbf{a}_B(\theta'_p, \alpha'_p)$ denote the $A_{\mathrm{BS}} \times 1$ array response vector (ARV) of the BS antenna system and $\mathbf{a}_U(\theta_p, \alpha_p)$ denote the $A_{\mathrm{UE}} \times 1$ ARV of the UE antenna system for a given cluster p. Here, (θ_p, α_p) and (θ'_p, α'_p) are the AoA and angle-of-departure (AoD) for cluster p, at the time of reception or transmission, respectively. Then, the $A_{\mathrm{UE}} \times A_{\mathrm{BS}}$ channel matrix $\mathbf{H}$ between the BS and the UE can be expressed as:

$$\mathbf{H} = \sum_{p=1}^{P} h_p \mathbf{a}_U(\theta_p, \alpha_p)\mathbf{a}_B^*(\theta'_p, \alpha'_p) \tag{5}$$

where $(.)^*$ denotes conjugate transpose operation, P is the number of clusters, and h_p is the gain of the pth cluster (a complex number).

The transmit and receive beamforming vectors for any desired direction can be computed offline and stored in codebooks at the Tx and the Rx. At any time during IA, when the BS is using a transmit beamforming vector $\mathbf{f}_i \in \mathbb{C}^{A_{\mathrm{BS}} \times 1}$ and UE is using a receive beamforming vector $\mathbf{q}_j \in \mathbb{C}^{A_{\mathrm{UE}} \times 1}$ (i and j are the indices of the beamforming vectors in their codebooks), we can represent the received signal y_{ij} as:

$$y_{ij} = \mathbf{q}_j^* \mathbf{H} \mathbf{f}_i s + \mathbf{q}_j^* \mathbf{n} \tag{6}$$

where s is the transmitted signal and $\mathbf{n} \in \mathbb{C}^{A_{\mathrm{UE}} \times 1}$ is a matrix whose entries are complex circularly-symmetric white Gaussian noise. Note that a given Tx beamformer $\mathbf{f}_i$ (also, a given Rx beamformer $\mathbf{q}_j$) specifies the values for the angles α and θ in the Tx (also, Rx) antenna weight $w_{m,n}$, computed in Section 3. Let $\mathbb{Q} = \{\mathbf{q}_1, \mathbf{q}_2, \cdots, \mathbf{q}_D\}$ denote the codebook of the Rx beamformer, where D is the maximum number of narrow beams that can be generated at the Rx (depends on the resolution of the phase shifters).

To find the optimal Rx beamformer for a given Tx beamformer, we define the precoded channel vector $\mathbf{g}_i \triangleq \mathbf{H}\mathbf{f}_i$, where $\mathbf{g}_i \in \mathbb{C}^{A_{\mathrm{UE}} \times 1}$. Then, $\mathbf{q}_j^* \mathbf{g}_i$ corresponds to measuring $\mathbf{g}_i$ with the Rx beam j. Using the codebook $\mathbb{Q}$, we can form a basis matrix $\mathbf{Q}$ whose jth row is given by $\mathbf{q}_j^*$, $j = 1, \cdots, D$. Then, D measurements for D different Rx beamformers and a given precoded channel $\mathbf{g}_i$ can be collected as $\mathbf{v} = \mathbf{Q}\mathbf{g}_i$, where $\mathbf{v}$ is a vector of length D, containing the channel measurement results. Our aim here is to reconstruct $\mathbf{v}$ by taking only r measurements from $\mathbf{g}_m$ where $r < D$, and find the beam IDs of these r measurements. From (5), the channel has P

clusters, meaning that $\mathbf{v}$ is P-sparse, i.e., it displays P peak values[1]. Hence, $\mathbf{v}$ can be constructed provided that $r \geq P$. Let us define $\mathbf{\Phi}$ as an $r \times D$ compressed measurement matrix. Then, output $\mathbf{\Psi}$ of the compressed measurement process can be represented as:

$$\mathbf{\Psi} = \mathbf{\Phi v} = \mathbf{\Phi Q g}_i = \mathbf{\Theta g}_i \qquad (7)$$

where $\mathbf{\Theta}$ is an $r \times A_{\text{UE}}$ matrix and $\mathbf{\Psi}$ is a column vector of length r. The problem is then reduced to designing a stable measurement matrix $\mathbf{\Phi}$ such that the key information in any P-sparse or compressible signal is not lost through the dimensionality reduction. In other words, we would like to reconstruct $\mathbf{v}$ by using the available measurement results $\mathbf{\Psi}$ and the known compressed measurement matrix $\mathbf{\Phi}$. A necessary and sufficient condition to find a solution to our problem for the P-sparse $\mathbf{v}$ is the restricted isometry property (RIP), which is satisfied by a given matrix $\mathbf{\Theta}$ if [10]

$$(1 - \epsilon) \leq \frac{\|\mathbf{\Theta z}\|_2^2}{\|\mathbf{z}\|_2^2} \leq (1 + \epsilon) \qquad (8)$$

holds for any arbitrary P-sparse $\mathbf{z}$ and for some isometry constant $\epsilon > 0$. Specifically, the matrix $\mathbf{\Theta}$ must preserve the length of an arbitrary P-sparse $\mathbf{z}$. A related condition, referred to as *incoherence*, requires that the rows of $\mathbf{\Phi}$ to not sparsely represent the columns of $\mathbf{Q}$. Both the RIP and incoherence can be achieved with high probability simply by selecting $\mathbf{\Phi}$ as a random matrix [10]. Specifically, when the entries of $\mathbf{\Phi}$ are drawn independently from a $\mathcal{N}(0, 1/r)$ distribution, $\mathbf{\Phi}$ can satisfy RIP and incoherence with high probability if $r \geq cP \log(D/P)$, where c is a small constant that depends on the desired probability of success. This result is summarized in the following theorem [10]:

THEOREM 1. *Let $r \geq cP \log(D/P)$ and construct $\mathbf{\Phi}$ by drawing its entries independently from a Gaussian distribution $\mathcal{N}(0, 1/r)$. Then, with probability exceeding $1 - e^{-cr}$, it is possible to reconstruct every P-sparse signal $\mathbf{v}$ of length D using $\mathbf{\Psi}$.*

Thus, the P-sparse $\mathbf{v}$ can be recovered from only $r \geq cP \log(D/P)$ random measurements. Generally, $\mathbf{\Phi}$ is constructed iteratively by adding a new random row at each iteration. However, the measurement matrix $\mathbf{\Phi}$ constructed with random phase shifts has low beamforming gains, which will likely not satisfy the link budget [21]. On the other hand, by selecting the rows of $\mathbf{\Phi}$ from the codebook $\mathbb{Q}$, the beamforming gains for any given direction can be maximized. To find which beamformers to select from $\mathbb{Q}$, Bayesian compressive sensing can be used [17]. With this approach, $\mathbf{\Phi}$ can be constructed such that at each iteration, a new row is selected from $\mathbb{Q}$ with the goal of reducing the uncertainty in the estimated $\mathbf{v}$. In step n, this is equivalent to selecting a row that maximizes the variance of the measurement result ψ_n, where ψ_n denotes the nth element of $\mathbf{\Psi}$. In other words, the new row $\mathbf{q}_i^*$ should be selected to constitute the measurement for which the data is most uncertain.

Using this, we next describe three algorithms that aim at determining the best beam directions for the BS and the UE. Because closeby beams give correlated results (and hence cannot maximize the variance of a new measurement), in each iteration, the algorithms probe a beam that points at a significantly different angle.

---

[1]In general, the notion of P-sparsity is used for vectors with at most P nonzero entries. However, as shown in [9], compressive sensing can be used to reconstruct noisy vectors with P peaks. Therefore, for convenience, we refer to vectors exhibiting P peaks as P-sparse.

5 PEAK-FINDING ALGORITHMS

In this section, we first develop two algorithms for 2D beam finding, and then we extend these algorithms to a 3D environment. The algorithms seek to identify the Rx beam j that yields the largest $|\mathbf{q}_j^* \mathbf{g}_i|^2$, i.e, the largest gain for a given precoded channel. In Section 5.1, we design an algorithm to find the best beam in the case of a single cluster. We extend this design to multiple clusters in Section 5.2. In Section 5.3, we modify the algorithms to work in a 3D environment. Finally, in Section 5.4, we discuss how to select the optimal design parameter K (number of angular regions).

5.1 Single-peak Finding (SPF) Algorithm

For now, we assume that the Tx is pointing towards a fixed, arbitrarily chosen direction using its beam i and beamformer $\mathbf{f}_i$. Rx tries to find the optimal beam w.r.t the given Tx direction. Extension to finding the optimal direction in the Tx side will be explained in Section 6. While pointing in a given direction i, the Tx sends synchronization signals and Rx measures the received power by steering its receive beam. For brevity, in this section, we omit the subscript i from $\mathbf{g}_i$. Note that for now, we consider a fixed elevation angle for both Tx and the Rx, and aim at finding the best azimuth angle for the Rx.

A typical plot of beam ID vs. SNR displays multiple peaks due to channel clusters. For now, we consider a single-peak scenario (see Fig. 1). Note that the graph in Fig. 1 cannot be perfectly reconstructed without measuring the SNR for each Rx beam. However, our aim is to find the peak by using only a subset of Rx beams, exploiting the previously presented CS analysis. Specifically, we aim at taking r measurements ($r < D$) such that the optimal Rx beamformer for a given Tx beamformer can be found with high probability (see Thm. 1).

Our proposed algorithm, called SPF, is a variation of binary search. First, the precoded channel $\mathbf{g}$ is measured using an Rx beamformer $\mathbf{q}_i$ that generates a starting beam i in the middle of the Rx field-of-view (FoV). From $\mathbf{q}_i$, we obtain $v_i = \mathbf{q}_i^* \mathbf{g}$. Then, i's left and right adjacent beams in the azimuth domain, $i - 1$ and $i + 1$, are scanned and $v_{i-1} = \mathbf{q}_{i-1}^* \mathbf{g}$ and $v_{i+1} = \mathbf{q}_{i+1}^* \mathbf{g}$ are obtained. If $|v_i|^2 > |v_{i-1}|^2$ and $|v_i|^2 > |v_{i+1}|^2$, where $|\cdot|$ indicates the modulus of a complex number, then v_i is the peak. Otherwise, $\mathbf{v}$ is "rising" towards the left or the right of beam i. Thus, the directions that $\mathbf{v}$ is not rising towards no longer need to be scanned. This leaves us with the subset of the codebook $\mathbb{Q}'$, where $\mathbb{Q}' = \mathbb{Q}\{1, \cdots, i - 1\}$ or $\mathbb{Q}' = \mathbb{Q}\{i + 1, \cdots, D\}$, eliminating the need to probe the directions in $\mathbb{Q}/\{\mathbb{Q}' \cup \{i\}\}$. Then, the procedure is repeated for the remaining directions in $\mathbb{Q}'$ until the peak is reached (see Algorithm 1). An example is illustrated in Fig. 1, where the numbers below the dots represent the order by which the beams are scanned.

If $\mathbf{v}$ exhibits a single peak, the SPF algorithm finds it in $O(\log D)$ time. However, if $\mathbf{v}$ has multiple peaks, SPF finds only one of the peaks, and not necessarily the optimal. To cope with that, we next propose the multiple-peak finding (MPF) algorithm.

5.2 Multiple-peak Finding (MPF) Algorithm

To reduce the chances of getting stuck at a local maximum, in the MPF algorithm, the codebook $\mathbb{Q}$ is divided into K equal-size subsets, each representing an angular region. Here, K is selected

---

Algorithm 1 Single-peak Finding Algorithm

1: **procedure** SINGLE_PEAK($\mathbb{Q}$, $\mathbf{g}$)
2: *Initialize*:
3:     $i \leftarrow D/2$
4:     $v_i \leftarrow \mathbf{q}_i^* \mathbf{g}$, $v_{i-1} \leftarrow \mathbf{q}_{i-1}^* \mathbf{g}$, $v_{i+1} \leftarrow \mathbf{q}_{i+1}^* \mathbf{g}$
5: *Recursion*:
6:     **if** $|v_i|^2 > |v_{i-1}|^2$ **and** $|v_i|^2 > |v_{i+1}|^2$ **then return** $|v_i|^2$
7:     **else if** $|v_i|^2 > |v_{i-1}|^2$ **and** $|v_i|^2 < |v_{i+1}|^2$ **then return**
    SINGLE_PEAK($\mathbb{Q}\{i + 1 : D\}$, $\mathbf{g}$)
8:     **else return** SINGLE_PEAK($\mathbb{Q}\{1 : i - 1\}$, $\mathbf{g}$)
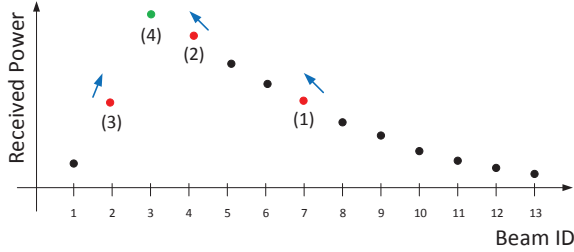

Figure 1: Received power vs. beam ID (single peak). Numbers below the dots represent the order by which the beams are scanned. Red dots correspond to intermediate beams and the green dot corresponds to the peak.

Algorithm 2 Multi-peak Finding Algorithm

1: **procedure** MULTI_PEAK($\mathbb{Q}$, $\mathbf{g}$, K)
2: *Divide Regions*:
3:     Divide $\mathbb{Q}$ into K equal regions R_i
4: *Finding Peaks*:
5:     Candidates $\Omega \leftarrow \{ \ \}$
6:     **for** Each R_i, $i \in \{1, \cdots K\}$ **do**
7:         localMax $\leftarrow$ SINGLE_PEAK(R_i, $\mathbf{g}$)
8:         $\Omega \leftarrow \Omega \cup$ localMax
    return max(Ω)

---

in a way that each region is likely to contain at most one peak. Then, the SPF algorithm runs within each region. Finally, the local maxima that are found at different regions are compared, and the largest among them is selected (see Algorithm 2). The complexity is $O(K \log \frac{D}{K})$, as the SPF algorithm is run in K regions, each of size $\frac{D}{K}$. Clearly, as K approaches D, the MPF algorithm converges to exhaustive search and the complexity approaches $O(D)$. On the other hand, if K is chosen very small (e.g., 1), the complexity is $O(\log D)$, but there is a high chance that the global maximum will be missed. If the local maxima that the algorithm returns cannot support the link budget, a misdetection is declared; otherwise the beam is declared "suboptimal" but communications along that beam can still be established. Thus, by choosing a proper K, we increase the chances of having at most one peak in each region, which the algorithm is guaranteed to find.

An example of the MPF algorithm is illustrated in Fig. 2. Here, the underlying channel has two clusters in the directions indicated by
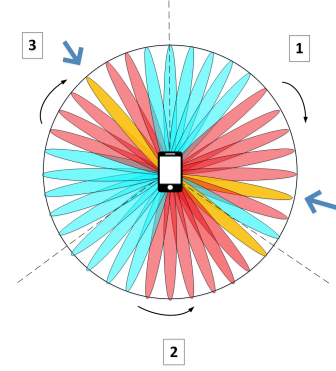

Figure 2: Example of executing the MPF algorithm. Straight arrows show clusters and curved arrows show rising directions. Red indicates that a beam is probed and yellow indicates that a beam is a candidate for the optimal direction.

the arrows. K is selected as 3. The boundaries of the K regions are indicated with dashed lines, dividing the whole codebook into three (numbered clockwise). The UE simply runs SPF for each region, first taking measurements from the middle beams at each region and their neighbors (scanned beams are shown in red). Using these measurements, the UE determines the rising directions, eliminating at least half of the beams in each region. Then, it scans through several more beams, until reaching the beams indicated with yellow. The yellow beams yield the highest measurement results within their regions, making them the three candidates for the optimal beam. Finally, MPF compares the three measurement results, and selects the beamformer corresponding to the highest result.

5.3   3DPF Algorithm

We now describe how the MPF algorithm can be extended to 3D beam search. In the 2D case, every time a beam direction i is probed, two adjacent beams in the azimuth domain, $i - 1$ and $i + 1$, are also probed. In the 3D case, each time beam direction i is probed, four adjacent beams are also probed: up and down in the elevation domain, and left and right in the azimuth domain. The main difference between MPF and 3DPF is that when finding the rising directions in 3D, we take measurements from these four neighbors of beam i and determine the rising quadrant (instead of the rising half of the array). Afterwards, the algorithm is run recursively in that quadrant. For a small D, measuring four neighbors may incur a large overhead. However, when D is relatively large, that overhead is negligible, as demonstrated in Section 7.

Similar to MPF, in 3DPF the space is divided into K angular regions to account for multiple peaks. Specifically, the horizontal domain is divided into K_x and the vertical domain is divided into K_y regions, where $K = K_x K_y$. As the algorithm still runs in logarithmic time within each region, the complexity is still $O(K \log \frac{D}{K})$.

The 3DPF is provided as a pseudocode in Algorithm 3. In Section 4, we denoted $\mathbf{q}$, $\mathbf{f}$ and $\mathbf{v}$ as vectors. In reality, when UPAs are used, they are flattened matrices. For consistency in the notation, here we keep using the vector notation. We use $v_{i,up}$, to refer to the measurement result obtained from i's upper neighboring beam in

---

Algorithm 3 3DPF Algorithm

1: **procedure** 3D_SINGLE_PEAK($\mathbb{Q}$, $\mathbf{g}$)
2:    *Initialize*:
3:      $i \leftarrow$ middle beam of $\mathbb{Q}$
4:      $v_i \leftarrow \mathbf{q}_i^* \mathbf{g}$
5:      $v_{i,left} \leftarrow \mathbf{q}_{i,left}^* \mathbf{g}$, $v_{i,right} \leftarrow \mathbf{q}_{i,right}^* \mathbf{g}$
6:      $v_{i,up} \leftarrow \mathbf{q}_{i,up}^* \mathbf{g}$, $v_{i,down} \leftarrow \mathbf{q}_{i,down}^* \mathbf{g}$
7:    *Recursion*:
8:      **if** $|v_i|^2 > |v_{i,up}|^2$ **and** $|v_i|^2 > |v_{i,down}|^2$ **and** $|v_i|^2 > |v_{i,left}|^2$ **and** $|v_i|^2 > |v_{i,right}|^2$ **then return** $|v_i|^2$
9:      **else if** $|v_i|^2 < |v_{i,up}|^2$ **and** $|v_i|^2 < |v_{i,right}|^2$ **then return** 3D_Single_Peak($\mathbb{Q}$\{upper-right quadrant\}, $\mathbf{g}$)
10:      **else if** $|v_i|^2 < |v_{i,up}|^2$ **and** $|v_i|^2 < |v_{i,left}|^2$ **then return** 3D_Single_Peak($\mathbb{Q}$\{upper-left quadrant\}, $\mathbf{g}$)
11:      **else if** $|v_i|^2 < |v_{i,down}|^2$ **and** $|v_i|^2 < |v_{i,right}|^2$ **then return** 3D_Single_Peak($\mathbb{Q}$\{lower-right quadrant\}, $\mathbf{g}$)
12:      **else return** 3D_Single_Peak($\mathbb{Q}$\{lower-left quadrant\}, $\mathbf{g}$)
13: **procedure** 3DPF($\mathbb{Q}$, $\mathbf{g}$, K_x, K_y)
14:    *Divide Regions*:
15:      Divide $\mathbb{Q}$ into K ($K = K_x K_y$) equal regions R_i
16:    *Finding Peaks*:
17:      Candidates $\Omega \leftarrow \{ \}$
18:      **for** Each R_i, $i \in \{1, \cdots K\}$ **do**
19:        localMax $\leftarrow$ 3D_SINGLE_PEAK(R_i, $\mathbf{g}$)
20:        $\Omega \leftarrow \Omega \cup$ localMax
       return max(Ω)

---

the elevation domain. Similar definitions apply to $v_{i,left}$, $v_{i,right}$, and $v_{i,down}$. The notation for $\mathbf{q}_i$ is extended the same way to account for four different neighboring beam directions.

5.4 Selecting the Optimal Number of Regions

As discussed in Section 4, the peaks of the P-sparse measurement vector $\mathbf{v}$ can be found with high probability using $r \geq cP \log(D/P)$ samples (probed narrow beams). Setting $K = P$ in the 3DPF algorithm yields $r = P \log \frac{D}{P}$ samples. As a result, for r to be greater than or equal to $cP \log(D/P)$, c must be equal to 1. Using Theorem 1, it is proven that with $K = P$, the 3DPF algorithm has a misdetection probability below $e^{-cr} = e^{-r}$.

Unfortunately, there is no way to know in advance how many clusters a given environment exhibits at a specific operating frequency. However, there exists several works addressing the distribution of the number of clusters in various mmW bands (e.g., [4, 16]). In this paper, we aim at accounting for a relatively large number of clusters to lower the chances of misdetection. Let P^* be the 95th-percentile of P. In [4], P is modeled as a random variable with distribution $\max\{Poisson(\mu), 1\}$, where $\mu = 1.8$, for the 28 GHz band. Solving numerically, $P^* \approx 3.72$ when the operating frequency is 28 GHz. We can then select $K = \lceil P^* \rceil$, where $\lceil . \rceil$ is the ceiling function. Note that in [4], P is modeled for a 2D channel. In our experiments, we observed that for 2D beam searching, selecting $K = 4$ achieves good performance in terms of discovery time and misdetection probability. For 3DPF, we tried several K values and found $K = 16$ to achieve very low misdetection rate and high probability of identifying the optimal beam.

6 FASTLINK PROTOCOL

In this section, we present our FastLink protocol for the IA process in mmW systems, and explain how it integrates the 3DPF algorithm as part of the message exchange between the BS and the UE.

In LTE systems, the IA procedure utilizes an omnidirectional signal called the Cell Reference Signal (CRS), which is regularly monitored by each UE to create a wideband channel estimate that can be used both for demodulating DL transmissions and for estimating the channel quality [14]. However, for 5G mmW systems, IA must take place directionally. As a result, when the main beams of the Tx and the Rx do not point to each other, the directional link cannot be established.

To find a suitable directional link, recent 5G specifications require that the BS covers the whole spatial area with a pre-configured number of beams, using periodically transmitted synchronization signal (SS) blocks [1]. These SS blocks carry primary synchronization signals (PSS), secondary synchronization signals (SSS), and physical broadcast channel (PBCH) information. PSS is mainly used for initial symbol boundary synchronization to the NR cell and the SSS is used for detection of cell and beam IDs. When the UE enters the coverage area of a BS, it listens to an SS burst (consisting of multiple SS blocks) and measures the signal quality of different beams. It then determines the beam for which the received power is maximum (and above a predefined threshold). This beam will be chosen for subsequent transmissions/receptions. After determining the best BS beam, the UE has to wait for the BS to schedule the random access channel (RACH) opportunity for the beam direction that the UE has selected. For each SS block, the BS will specify one or more RACH opportunities to occur in a certain time, frequency, and direction, so that the UE knows when to transmit the RACH preamble [14]. During a RACH opportunity, UE performs random access, implicitly informing the BS of its selected beam direction. Note that the existing 5G specifications do not standardize how beam sweeping will be performed at the UE.

Our 3DPF algorithm can be directly applied at the UE side, without changing the default 5G IA process. This reduces the search time at the UE side, but the BS still sweeps its beams exhaustively. With some small changes in the IA structure, 3DPF can be employed at both the BS and the UE. In FastLink, the BS and the UE both sequentially scan a small subset of their beam directions. Specifically, during an SS block, the BS steers its beam towards a direction and transmits PSS and SSS. During this SS block, the UE constantly measures the received power, steering its receive beam according to the 3DPF algorithm. At the end of the SS block, the BS switches to Rx mode, and listens to a REPLY message from the UE along the same beam direction. UE sends its REPLY using the best beam direction it found for the given BS beam. After measuring the Rx power, in the next SS block, the BS steers its beam towards another direction suggested by 3DPF, and the UE runs a new search for the new BS beam. Measurements of received powers of REPLY messages are stored in a table at the BS. In the last stage of 3DPF, BS selects the beam with the highest power.

For a time division duplex (TDD) system, the BS and UE operate on the same frequency, and so the number of clusters they experience are the same. Thus, the optimal K for the BS and the UE are the same, i.e. $K_{BS} = K_{UE} = \lceil P^* \rceil$, as discussed in Section 5.4. This
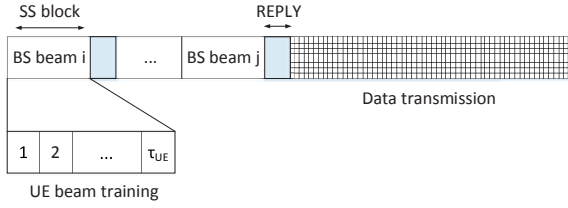
Figure 3: Proposed transmission block structure.

allows the BS to know how long each SS block should last (for UE to run 3DPF), without prior communication with the UE.

The transmission block structure for FastLink is shown in Fig. 3. BS sends PSS and SSS for τ_{UE} consecutive mini-slots within an SS block through a selected beam i, where τ_{UE} is the maximum required number of mini-slots for the UE to run 3DPF algorithm with the pre-selected K. Specifically, $\tau_{UE} = \lceil P^* \rceil \log \frac{D_{UE}}{\lceil P^* \rceil}$, where D_{UE} is the maximum number of narrow beams at the UE. Then, the UE determines the best receive beam for BS transmit beam i and sends a REPLY message to the BS. However, the power of the signal received by the BS can be lower than its sensitivity. If the BS does not receive a REPLY message from the UE after τ_{UE} mini-slots, it stores a minimum power value, ζ, in its table for beam i. Then, the BS continues executing 3DPF, selecting the next transmit beam suggested by the algorithm according to the received power value. In total, BS needs to scan at most $\tau_{BS} = \lceil P^* \rceil \log \frac{D_{BS}}{\lceil P^* \rceil}$ beams, where D_{BS} is the maximum number of narrow beams at the BS. After collecting all REPLY messages from the UE for the selected beams, the BS finally selects the best transmit beam from the table and the UE selects the best receive beam for the given transmit beam. This way, the time required to establish a directional link can be reduced from $D_{BS}D_{UE}$ to $\tau_{BS}\tau_{UE}$ ($\tau_{BS} \ll D_{BS}$ and $\tau_{UE} \ll D_{UE}$).

7   PERFORMANCE EVALUATION

In this section, we evaluate the performance of 3DPF through extensive hardware experiments and computer simulations. We compare 3DPF with 802.11ad beam search approach, in which the search time scales linearly with D. Note that current 5G NR beam search also scales linearly with D, attaining similar results to 802.11ad.

7.1   Experimental Results

We first conduct extensive experiments to verify the efficiency of 3DPF. 4×4 UPAs are used in our experiments with $d_x = 0.5\lambda$ and $d_y = 0.6\lambda$. For the sake of measuring the received power, a continuous wave with 5 dBm amplitude is transmitted over the 29 GHz band, which is a candidate band for 5G communications. To generate the waveform, Keysight E8257D-ATO-8384 PSG signal generator is used. At the Rx side, the array is connected to Keysight PXA-550-MY55002004 vector signal analyzer (VSA). To steer the transmit/receive beams to desired directions, antenna arrays are connected to microcontrollers, which are interfaced with the PC through serial port. The whole setup with the Tx, Rx, PSG, and the VSA can be seen in Fig. 4.

In the experiments, Tx direction is fixed and the best Rx direction for that fixed Tx direction is determined using 802.11ad beam scan and the 3DPF algorithm. We test several LOS and NLOS scenarios
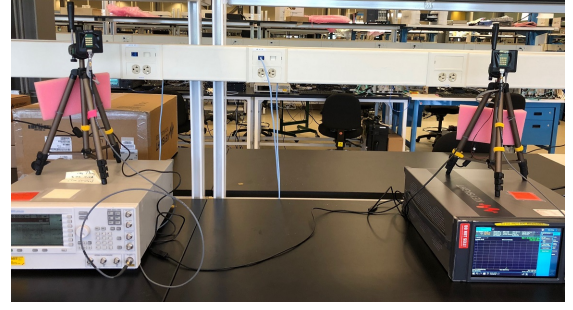

Figure 4: Test setup using 4×4 UPAs both at the Tx and the Rx side, signal generator and vector signal analyzer.
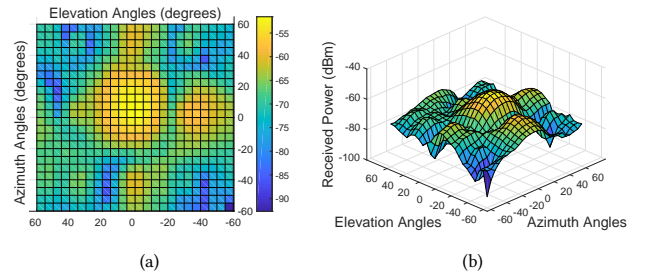

Figure 5: Rx powers for different beam directions at 29 GHz operating frequency and under first scenario (Tx-Rx separation of 3 m). (a) Flattened, (b) 3D representation.

with a Tx-Rx separation of 3 m, where the NLOS path is created by a 1.2 m × 1.2 m metal reflector. The effective beam scanning range of the UPAs in our experiments are ±60° from broadside, in both azimuth and elevation (effective FOV = ∼ 120° in each direction). Beyond that, the antenna gain drops significantly as a result of the non-ideal behavior of the antenna elements. Therefore, this region can be considered as one quasi-omni beam for the sector-level scanning phase of 802.11ad, and thus in the beam refinement phase, 802.11ad protocol exhaustively scans all narrow beams in this region. To obtain the AoA profile, we exhaustively scanned the 3D space within the effective beam scanning range of the antenna arrays under different scenarios. Using the above setup, we collected RSS measurements from the 3D space (see Fig. 5).

In addition to exhaustively probing all directions, we also implemented our 3DPF algorithm in the Rx side. Next, we compare 3DPF with 802.11ad/exhaustive beam search approach and plot the percentage of the scanned beams and actual elapsed time. We varied K to study the resulting time overhead. The results are shown in Fig. 6. As shown in Fig. 6(b), even when $K = 25$, the time required to find the best beam is still 70% less than that of 802.11ad. Note that in Fig. 6(b), the y-axis on the left shows the percentage of scanned directions, and the y-axis on the right shows the actual elapsed time (they are in one-to-one correspondence). Trials refer to different runs of the experimental scenarios.

In Fig. 6(a), an angular step size of 1° is used, which results in $D = 14641$. On the other hand, in Fig. 6(b), a larger step size of 5° is used, which results in $D = 625$. Note that when switching between beams, we impose an artificial delay to accommodate the
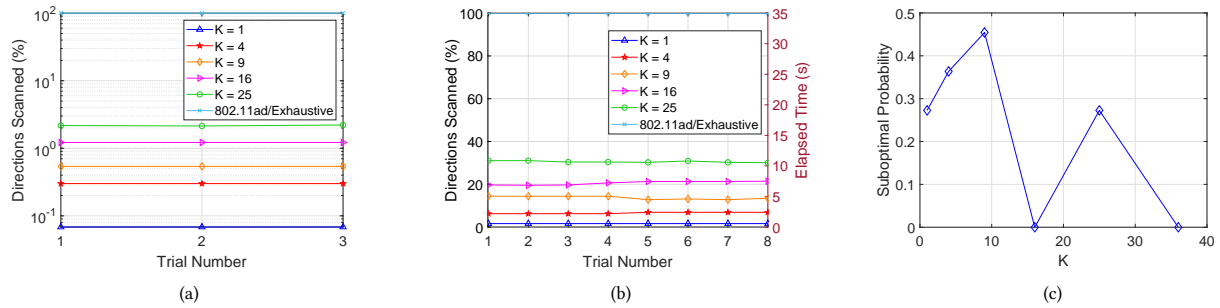
Figure 6: Performance comparison of the 3DPF algorithm and 802.11ad/exhaustive beam scan. (a) Percentage of scanned beams and elapsed time vs. trial number for $1°$ resolution, (b) percentage of scanned beams and elapsed time vs. trial number for $5°$ resolution, (c) probability of finding a suboptimal beam pair in 3DPF algorithm (averaged over 11 trials).

time needed to read the Rx power value from the VSA through the serial port. For that reason, the measured latency values in Fig. 6(b) are higher than the actual beam scanning delay. Another important observation is regarding the overhead of scanning the neighbors in 3DPF. In Fig. 6(a), the search space is very large, so the overhead of scanning the neighbors is negligible. Thus, 3DPF scans less than 1% of all the beams, on average. However, when the search space is smaller, the overhead is more pronounced. Nevertheless, 3DPF still scans $2\% - 30\%$ of the space, depending on the selected K.

Recall that, as explained in Section 5.2, if the beam that 3DPF returns cannot support the link budget, a misdetection is declared; otherwise if the beam does not yield the highest Rx power but communications along that beam can still be established, the beam is declared "suboptimal". Due to short Tx-Rx separation, no misdetection was observed in any of our experiments. However, the channel between the Tx and the Rx changes slightly between different runs of the same scenario. We assumed that deviations that are within $5°$ from the optimal beam direction do not cause a suboptimal beam selection. However, any deviation larger than that is declared suboptimal, and the probability of finding a suboptimal beam vs. K is shown in Fig. 6(c).

7.2 Simulation Results

Due to the limitations of our experimental setup, we rely on computer simulations to study the impact of Tx-Rx distance. Here, Tx power is set to $P_{Tx} = 30$ dBm and $A_{BS} = A_{UE} = 16$. We run our simulations in the 28 GHz band with UPAs ($d_x = d_y = \lambda/2$), using [4] to model large-scale effects. For small-scale effects, we place random scatterers on an ellipsoid between the Tx and the Rx. Tx beam is kept the same, and Rx sweeps its beam in $5°$ steps to find the best receive direction for the given Tx beam. Beam scanning range is kept the same as in the hardware experiments ($±60°$ from broadside, in both azimuth and elevation). Tx-Rx separation varies between 10 m and 250 m. Results are averaged over 1000 runs. An example simulation setup is seen in Fig. 7(a), and the resulting Rx powers for different Rx beam directions are shown in Figs. 7(b) and 7(c). The results from the simulations are in line with those obtained in the hardware experiments. In Fig. 8(a), for all values of K, the number of scanned directions under 3DPF is significantly smaller

than that of 802.11ad. Even when $K = 25$, 3DPF scans less than 35% of the directions scanned by the exhaustive approach. In Fig. 8(b), we observe the misdetection probability vs. Tx-Rx distance. Except when $K = 1$, the difference in the misdetection probability between 3DPF and 802.11ad is negligible. Finally in 8(c), suboptimal probability is plotted vs. distance. Although 3DPF has a high suboptimal probability when K is small, the suboptimal probability decreases significantly when $K \geq 9$. Note that suboptimal probability decays with increasing distance, as the misdetection probability becomes dominant.

8 CONCLUSIONS

In this paper, we proposed FastLink, an efficient beam finding protocol for mmW systems that always transmits using the narrowest possible beams, allowing high beamforming gains and low misdetection rate. We first formulated the beam finding problem as a sparse problem, and used CS to determine the minimum number of measurements needed to reconstruct the peaks of the sparse channel. Using CS analysis, we designed the 3DPF algorithm and show that it significantly reduces the search latency compared to existing search schemes. 3DPF was incorporated into an IA protocol called FastLink to allow the BS and the UE to establish a directional link. Finally, extensive experimental and simulation results were provided to verify the efficiency of 3DPF.

REFERENCES
[1] 3GPP TR 38.802 v14.2.0. 2017. Study on New Radio Access Technology-Physical Layer Aspects (Release 14). http://www.3gpp.org/ftp//Specs/archive/38_series/38.802/38802-e20.zip

(a)   (b)   (c)
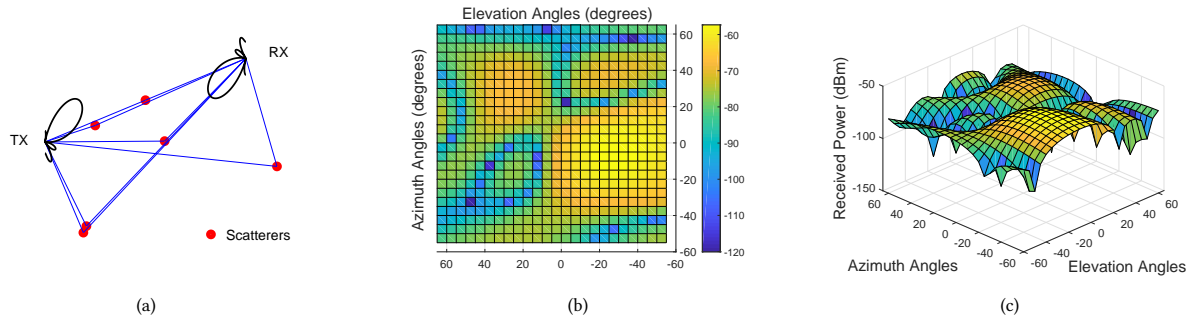
Figure 7: (a) Example projection of the 3D simulation environment on X-Y plane with random scatterers and UPAs both at Tx and Rx, (b) flattened received power with Tx-Rx separation of 100 m and $P_{\text{Tx}} = 30$ dBm, (c) 3D representation of the received power along various beam directions.

(a)   (b)   (c)
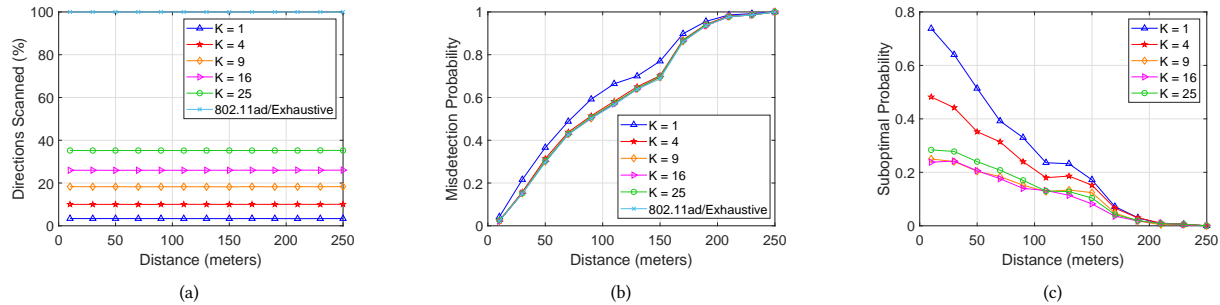
Figure 8: Simulation-based comparison between 3DPF and 802.11ad search. (a) Directions scanned vs. distance, (b) misdetection probability vs. distance, (c) suboptimal probability vs. distance.

[2] Omid Abari, Haitham Hassanieh, Michael Rodriguez, and Dina Katabi. 2016. Millimeter wave communications: From point-to-point links to agile network connections. In *Proc. of the 15th ACM Workshop on Hot Topics in Networks*. Atlanta, GA, 169–175.

[3] Ahmed Abdelreheem, Ehab Mahmoud Mohamed, and Hamada Esmaiel. 2018. Location-Based Millimeter Wave Multi-Level Beamforming Using Compressive Sensing. *IEEE Commun. Lett.* 22, 1 (2018), 185–188.

[4] Mustafa Riza Akdeniz, Yuanpeng Liu, Mathew K. Samimi, Shu Sun, Sundeep Rangan, Theodore S. Rappaport, and Elza Erkip. 2014. Millimeter wave channel modeling and cellular capacity evaluation. *IEEE J. Sel. Areas Commun.* 32, 6 (2014), 1164–1179.

[5] Ahmed Alkhateeby, Geert Leusz, and Robert W. Heath. 2015. Compressed sensing based multi-user millimeter wave systems: How many measurements are needed?. In *Proc. of the IEEE ICASSP*. South Brisbane, Australia, 2909–2913.

[6] Jeffrey G. Andrews, Stefano Buzzi, Wan Choi, Stephen V. Hanly, Angel Lozano, Anthony C.K. Soong, and Jianzhong Charlie Zhang. 2014. What will 5G be? *IEEE J. Sel. Areas Commun.* 32, 6 (2014), 1065–1082.

[7] Tianyang Bai, Ahmed Alkhateeb, and Robert W. Heath. 2014. Coverage and capacity of millimeter-wave cellular networks. *IEEE Commun. Mag.* 52, 9 (2014), 70–77.

[8] Waheed U. Bajwa, Jarvis Haupt, Akbar M. Sayeed, and Robert Nowak. 2010. Compressed channel sensing: A new approach to estimating sparse multipath channels. *Proc. of the IEEE* 98, 6 (2010), 1058–1076.

[9] Emmanuel J. Candes. 2008. The restricted isometry property and its implications for compressed sensing. *Comptes rendus mathematique* 346, 9-10 (2008), 589–592.

[10] Emmanuel J. Candes and Terence Tao. 2005. Decoding by linear programming. *IEEE Trans. Inf. Theory* 51, 12 (2005), 4203–4215.

[11] Jinho Choi. 2015. Beam selection in mm-Wave multiuser MIMO systems using compressive sensing. *IEEE Trans. Commun.* 63, 8 (2015), 2936–2947.

[12] Omar El Ayach, Sridhar Rajagopal, Shadi Abu-Surra, Zhouyue Pi, and Robert W. Heath. 2014. Spatially sparse precoding in millimeter wave MIMO systems. *IEEE Trans. Wireless Commun.* 13, 3 (2014), 1499–1513.

[13] Marco Giordani, Marco Mezzavilla, C. Nicolas Barati, Sundeep Rangan, and Michele Zorzi. 2016. Comparative analysis of initial access techniques in 5G mmWave cellular networks. In *Proc. of the IEEE CISS*. Princeton, NJ, 268–273.

[14] Marco Giordani, Michele Polese, Arnab Roy, Douglas Castor, and Michele Zorzi. 2018. A Tutorial on Beam Management for 3GPP NR at mmWave Frequencies. *arXiv preprint arXiv:1804.01908* (2018).

[15] Morteza Hashemi, C. Emre Koksal, and Ness B. Shroff. 2018. Out-of-Band Millimeter Wave Beamforming and Communications to Achieve Low Latency and High Energy Efficiency in 5G Systems. *IEEE Trans. Commun.* 66, 2 (2018), 875–888.

[16] IEEE Computer Society. 2014. IEEE Standard-Part 11: Wireless LAN medium access control (MAC) and physical layer (PHY) specifications Amendment 3: Enhancements for very high throughput in the 60 GHz band (adoption of IEEE Std 802.11ad-2012). https://standards.ieee.org/findstds/standard/802.11ad-2012.html

[17] Shihao Ji, Ya Xue, and Lawrence Carin. 2008. Bayesian compressive sensing. *IEEE Trans. Signal Process.* 56, 6 (2008), 2346–2356.

[18] Sundeep Rangan, Theodore S. Rappaport, and Elza Erkip. 2014. Millimeter-wave cellular wireless networks: Potentials and challenges. *Proc. of the IEEE* 102, 3 (2014), 366–385.

[19] Theodore S. Rappaport, Shu Sun, Rimma Mayzus, Hang Zhao, Yaniv Azar, Kevin Wang, George N. Wong, Jocelyn K. Schulz, Mathew Samimi, and Felix Gutierrez. 2013. Millimeter wave mobile communications for 5G cellular: It will work! *IEEE Access* 1 (2013), 335–349.

[20] Wonil Roh, Ji-Yun Seol, Jeongho Park, Byunghwan Lee, Jaekon Lee, Yungsoo Kim, Jaeweon Cho, Kyungwhoon Cheun, and Farshid Aryanfar. 2014. Millimeter-wave beamforming as an enabling technology for 5G cellular communications: Theoretical feasibility and prototype results. *IEEE Commun. Mag.* 52, 2 (2014), 106–113.

[21] Daniel Steinmetzer, Daniel Wegemer, Matthias Schulz, Joerg Widmer, and Matthias Hollick. 2017. Compressive Millimeter-Wave Sector Selection in Off-the-Shelf IEEE 802.11ad Devices. In *Proc. of the 13th ACM CoNEXT*. Seoul, South Korea, 414–425.

[22] Anfu Zhou, Leilei Wu, Shaoqing Xu, Huadong Ma, Teng Wei, and Xinyu Zhang. 2018. Following the Shadow: Agile 3-D Beam-Steering for 60 GHz Wireless Networks. In *Proc. of the IEEE INFOCOM*. Honolulu, HI.